Ecological Indicators 178 (2025) 114114

Contents lists available at ScienceDirect

Ecological Indicators

journal homepage: www.elsevier.com/locate/ecolind

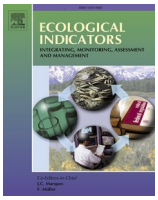

Original Articles

A novel environmental indicator: Compound wind droughts and heat waves for assessing climate-driven ecological and energy sustainability

Jiewen You [a,b,c], Fangxu Yin [a], Boen Zhang [d], Mo Zhou [e], Yamin Qing [e], Ying Chen [a,b,c], Lu Gao [a,b,c,*]

[a] School of Geographical Sciences, Fujian Normal University, Fuzhou, China
[b] Key Laboratory for Humid Subtropical Eco-geographical Processes of the Ministry of Education, Fujian Normal University, Fuzhou, China
[c] Fujian Provincial Engineering Research Center for Monitoring and Assessing Terrestrial Disasters, Fujian Normal University, Fuzhou, China
[d] School of Geography and the Environment, University of Oxford, Oxford, UK
[e] Department of Land Surveying and Geo-Informatics, The Hong Kong Polytechnic University, Hong Kong, China

ARTICLE INFO

Keywords:
Compound wind droughts and heat waves
Interpretable machine learning
Wind energy reliability
Ecological vulnerability

ABSTRACT

Compound extremes, specifically concurrent low wind power (wind droughts) and heat waves, threaten ecological stability and renewable energy. However, their dynamics and impacts remain poorly understood. This study introduces compound wind droughts and heat waves (WDHW) indicator to assess their patterns in mainland China from 2000 to 2022. Using observational data and explainable machine learning (XGBoost and SHAP), we analyzed the spatiotemporal distributions, underlying drivers, and ecological implications of WDHW. Results reveal spatial heterogeneity, with high-frequency WDHW (>70 cumulative days) concentrated in northwestern China and a national increase in event frequency within affected regions (0.042 d yr^{-1}). The XGBoost model performed well, with R^2 values of 0.88, 0.83, and 0.84 for training, cross-validation, and test datasets, respectively. SHAP analysis highlights maximum temperature (Tmax; SHAP = 0.722) and vapor pressure deficit (VPD; SHAP = 0.698) as primary drivers, with their interaction (SHAP = 0.321) demonstrating how heat and dryness link with 100-m hub-height winds. Ecological analysis shows peak WDHW frequencies in Half Protected ecoregions (28.8 days) and Deserts & Xeric Shrublands biomes (28.75 days), indicating dual vulnerabilities to biodiversity and energy systems. This study advances understanding of concurrent wind droughts and heat waves, providing implications for sustainable ecological and energy adaptation strategies.

1. Introduction

Wind energy has emerged as a pivotal renewable energy source globally, offering a sustainable pathway to decarbonize energy systems (McElroy et al., 2009; Lu et al., 2009; Antonini et al., 2024; Davis et al., 2018). This is especially critical for China, the world's largest wind energy producer with a cumulative installed capacity exceeding 470 GW by 2023. However, wind power generation, inherently determined by wind speed and proportional to its cube (Leahy and McKeogh, 2013; Pryor et al., 2020), is highly sensitive to atmospheric variability and climate change (Bloomfield et al., 2020; Grams et al., 2017; Xu et al., 2024). This vulnerability manifests acutely during heat waves, where persistent high-pressure systems suppress wind speeds, triggering prolonged wind-resource deficits (wind droughts) with surging electricity demand from cooling systems (ECMWF, 2021; Lledó et al., 2018).

Such compound wind droughts and heat waves create a dual energy crisis: constrained wind power supply converges with peak cooling demand. Heat waves drive surging electricity demand due to increased reliance on air conditioning and industrial cooling systems, while simultaneously degrading transmission efficiency (Ke et al., 2016; Lubega and Stillwell, 2018). The stagnant atmospheric conditions during heat waves reduce wind speeds, further curtailing wind power generation. This convergence of elevated demand and constrained supply exacerbates energy shortages (Graczyk et al., 2024; Liu et al., 2023b). These challenges can generate systemic risks that cascade beyond energy systems and threaten agricultural productivity, food security, and public health in warming climates (Hultgren et al., 2025; Shmelev et al., 2021; You et al., 2025). These compound events are exacerbated by climate projections indicating increased frequency and intensity of heat waves, which amplify the risks of concurrent wind

* Corresponding author.
E-mail address: l.gao@foxmail.com (L. Gao).

https://doi.org/10.1016/j.ecolind.2025.114114
Received 16 June 2025; Received in revised form 17 August 2025; Accepted 22 August 2025
Available online 25 August 2025

energy deficits and surging electricity demand, thereby underscoring the urgency of addressing these compound risks (Speizer et al., 2022; Tobin et al., 2018).

While previous studies have explored renewable energy resilience under climate extremes (Molina et al., 2023; Perera et al., 2020; Zhao et al., 2024), systematic assessments of wind power vulnerabilities during heat waves in China are scarce. China's distinct wind climatology and region-specific heat wave patterns underscore unique spatiotemporal risks to ecological and energy systems. The compound dynamics of wind droughts and heat waves (WDHW) events, particularly in regions facing intense climate stress, remain underexplored as environmental indicators. Moreover, the nonlinear interactions between temperature anomalies and wind speed variability demand deeper investigation to develop robust WDHW indicators.

Here, we established a new environmental indicator of compound WDHW for monitoring climate-driven stress on environmental and energy systems in China. Using high-resolution gridded observational data from 2000 to 2022, we analyzed the spatiotemporal patterns of wind energy distributions, heat wave frequency, and WDHW co-occurrence across mainland China. We employed XGBoost and SHAP (SHapley Additive exPlanation) to quantify temperature-wind speed dynamics, identifying key drivers and nonlinear interactions linking temperature anomalies to wind speed variability. Our findings highlight WDHW as a critical indicator of climate impacts, revealing spatial heterogeneity and increasing frequency in affected regions. This interpretable machine learning framework enhances understanding of climate-ecosystem interactions, supporting adaptive strategies for ecological sustainability and resilient wind energy systems in a warming climate.

2. Methods

2.1. Datasets

This study utilized daily mean wind speed, temperature, and maximum temperature data derived from the CN05.1 climate dataset. The dataset provides continuous coverage over mainland China at a spatial resolution of 0.25° × 0.25°. The dataset is based on quality-controlled observations from over 2,400 meteorological stations, with missing or inconsistent records filtered through rigorous quality control. Interpolation was performed using an "anomaly approach", which combines thin-plate spline interpolation of climatology with angular-distance weighted daily anomalies (Wu et al., 2017; Wu and Gao, 2013; Xu et al., 2009). The CN05.1 gridded daily meteorological dataset has been widely adopted for analyzing observed climate characteristics and evaluating model performance across China (Su et al., 2018; Wang et al., 2023; Wang and Yuan, 2023). Further details on data quality control, completeness, and interpolation methodology are provided in Text S1 of the Supporting Material. Given data availability and China's rapid wind energy expansion alongside significant climate change over the past two decades, this study analyzed the period from January 1, 2000, to December 31, 2022 (23 years), examining recent evolutions of wind energy characteristics and heat wave patterns under a warming climate. Consistent with previous study (Wang et al., 2025), we divided China into seven power zones (Northwest, North, Northeast, Central, East, South, Tibet), as shown in Fig. S1 in Supporting Material.

2.2. Conversion of wind speeds at hub height and calculation for wind power density

To align meteorological observations with wind turbine operational requirements, this study converts 10-m wind speeds (the standard measurement height) to 100-m hub heights using the power law wind profile. Following previous research (Liu et al., 2019), the relationship is expressed as:

$$v_{\mathrm{hub}} = v_{10}\left(\frac{h_{\mathrm{hub}}}{h_{10}}\right)^{\alpha} \tag{1}$$

$$\alpha = \frac{0.37 - 0.0881\cdot\ln v_{10}}{1 - 0.0881\cdot\ln\left(\frac{h_{10}}{10}\right)} \tag{2}$$

where v_{10} is the observed wind speed at 10 m (h_{10}), v_{hub} is the extrapolated speed at hub height (h_{hub} = 100 m), and α is the wind shear exponent. The exponent α is calculated using the empirical formula.

Substituting Eq. (2) into Eq. (1) yields the final conversion equation:

$$v_{\mathrm{hub}} = 10^{(0.37-0.0881\cdot \ln v_{10})}\cdot v_{10} \tag{3}$$

To evaluate regional variations in harvestable wind energy, wind power density (WPD) was employed as a key metric for estimating the theoretical energy yield of wind turbines (Antonini et al., 2024; You et al., 2025). WPD represents the kinetic energy flux available for conversion per unit rotor area (W m^{-2}), integrating wind speed magnitude and air density. These are the two primary factors governing energy extraction efficiency. Daily WPD values at 100 m height (aligned with modern turbine hub specifications) were calculated for each grid cell using the relationship:

$$\mathrm{WPD} = 0.5\left(\frac{p}{RT}\right)v_{hub}^{3} \tag{4}$$

where p denotes the surface pressure (Pa); R denotes the specific gas constant for dry air; T denotes 2-m air temperature (K); v_{hub} denotes the wind speed (m s^{-1}) at hub height.

2.3. Definition and identification of wind droughts, heat waves, and compound WDHW events

As shown in Fig. 1, wind droughts (WD), also referred to as wind-resource droughts (Liu et al., 2023a), are defined as periods of persistently low wind speeds that lead to a significant reduction in WPD and consequently, wind energy availability. This concept is analogous to meteorological drought but applied to wind resources, where anomalously low wind conditions persist over days to weeks, disrupting wind energy generation. In this study, we adopt the term 'wind drought' to emphasize its relevance to energy system impacts, in line with terminology used in recent literature (Antonini et al., 2024; Li et al., 2024). Wind droughts are identified when two criteria coincide: anomalously low WPD and wind speeds that are inadequate for turbine operation. Daily WPD values should fall below the 10th percentile threshold relative to historical daily climatological distributions, reflecting periods of substantially diminished wind energy potential. Simultaneously, wind speeds must remain below the industry-standard cut-in threshold of 3 m s^{-1}, i.e., the minimum required to initiate electricity generation in most wind power plants. These dual criteria capture both the physical scarcity of wind resources and the operational constraints of wind energy infrastructure.

A heat wave (HW) is characterized by a minimum of three consecutive days where the daily maximum temperature (Tmax) exceeds the 90th percentile of historical values for the corresponding calendar date (Fig. 1) (Perkins-Kirkpatrick and Lewis, 2020; You and Wang, 2021). To account for seasonal variability, percentile thresholds were derived using a 15-day moving window across the 2000–2022 climatological baseline, ensuring local thermal extremes are contextualized within regional climate norms. Additionally, a secondary threshold, i.e., the 75th percentile of Tmax, was applied to dynamically define the "summer season" by identifying the hottest 25 % of days annually, irrespective of calendar months. This adaptive approach replaces traditional seasonal boundaries (e.g., June–September) and accommodates China's diverse climatic zones, enabling spatially explicit detection of heat wave periods.

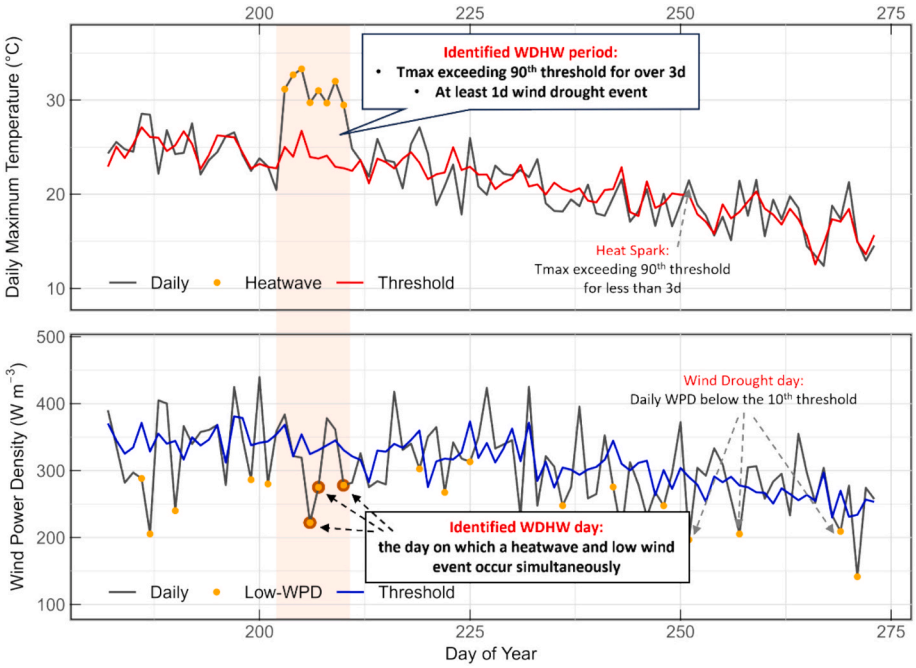

Fig. 1. Identification of compound wind drought and heat wave (WDHW) event periods and WDHW event days.

Compound wind droughts and heat waves (WDHW) serve as environmental indicators, defined by the spatial and temporal co-occurrence of extreme heat and wind droughts within the same grid cell, with at least one overlapping day. These events exert synergistic stress on ecological and wind energy systems, reflecting climate-driven vulnerabilities. We investigate WDHW frequency, spatial exposure, and magnitude to quantify their impacts, advancing monitoring strategies for ecological sustainability and resilient energy systems in China. Fig. 1 demonstrates the identification of WDHW events. The WDHW event period is identified when a heat wave witness at least one WD day, as indicated by the brown-shaded region. While a WDHW event days are specific days within this period when both conditions are met, marked by brown circles in the Fig. 1.

2.4. Trend detection and significance test

The study analyzed trends in the frequencies of WD, HW, and WDHW events, both spatially and annually, to understand changes over time and across regions using the Mann-Kendall (MK) test and Sen's slope estimator (Gilbert, 1987; Kendall, 1975; Mann, 1945). The non-parametric MK test detects monotonic trends, whether event frequencies consistently rise or fall, without requiring normally distributed data. This is particularly important for our climate data, which often exhibit variability and non-linear patterns. The MK test assesses significance at a 95 % confidence level, meaning trends are considered statistically significant if there is less than a 5 % chance the observed trend is due to random variation. Sen's slope estimator complements the MK test by quantifying the magnitude of the trend, providing a rate of change, such as how much the frequency of WDHW events increases or decreases per year. This method calculates the median slope of all pairwise differences in the time series, offering a robust rate of change per year for event frequencies, even with outliers common in climate data, which is widely used in previous research (You et al., 2024).

2.5. Interpretable machine learning for 100-m hub heights wind speed during WHDW periods

2.5.1. XGBoost

To explore the nonlinear relationship between environmental factors and 100-m hub heights wind speed during WHDW periods, we utilized the eXtreme Gradient Boosting (XGBoost) machine learning model (Chen and Guestrin, 2016). XGBoost is an advanced implementation of gradient boosting machines and an ensemble learning technique, which approach iteratively integrates multiple weak predictive models, typically decision trees, to form a robust, unified model (Bentéjac et al., 2019; Mitchell et al., 2018). The XGBoost model aims to minimize a regularized loss function of the form:

$$\mathrm{L}(\phi) = \sum_{i=1}^{n} l(y_i, \hat{y}_i) + \sum_{k=1}^{K} \Omega(f_k) \tag{5}$$

$$\Omega(f_k) = \gamma T + \frac{1}{2}\lambda |w|^2 \tag{6}$$

where $l(y_i, \hat{y}_i)$ denotes the loss between the observed y_i and predicted $\hat{y}_i$ wind speeds. $\Omega(f_k)$ is a regularization term penalizing the complexity of each regression tree f_k. Here, T is the number of leaves in the tree, w is the leaf score vector, γ and λ are regularization parameters, and λ is the number of trees.

The dataset used in this study is cleaned by removing incomplete cases, followed by an 80 %-20 % stratified train-test split. Recursive Feature Elimination method is used for feature selection, with 5-fold cross-validation applied to determine the optimal set of features. The XGBoost model then is trained with hyperparameter tuning via grid search, evaluating performance based on Root Mean Square Error (RMSE). Model validation was conducted using 5-fold cross-validation to ensure robustness and minimize overfitting. The full descriptions of preprocessing, hyperparameter, computational configuration and out-of-sample validation are included in Supporting Material (Fig. S2, Fig. S3, Text S2 and Text S3). We evaluated model performance for on the training dataset, cross-validation and test datasets using standard metrics, including RMSE, Mean Absolute Error (MAE), and the Coefficient of Determination (R^2).

RMSE measures the square root of the average of squared differences between predicted and observed values:

$$\mathrm{RMSE} = \sqrt{\frac{1}{n}\sum_{i=1}^{n}(y_i - \hat{y}_i)^2} \tag{7}$$

MAE measures the average magnitude of the absolute errors:

$$\mathrm{MAE} = \frac{1}{n}\sum_{i=1}^{n}|y_i - \hat{y}_i| \tag{8}$$

R^2 represents the proportion of variance in the observed data explained by the model:

$$R^2 = 1 - \frac{\sum_{i=1}^{n}(y_i - \hat{y}_i)^2}{\sum_{i=1}^{n}(y_i - \bar{y})^2} \tag{9}$$

where y_i is the observed wind speeds and $\hat{y}_i$ is the predicted wind speeds. $\bar{y}$ is the mean of observed wind speeds and n is the total number of samples.

In this study, we designated wind speed during WHDW periods as the dependent variable and developed XGBoost models to investigate its relationship with several features that represent both environmental conditions and heat wave intensity-related measures. These features include Tmax (maximum temperature) and VPD (Vapor Pressure Deficit), which are key environmental variables. Additionally, we contain lagged variables of Tmax (such as TmaxL1, TmaxL2, etc.), which capture the previous values of maximum temperature up to a 5-day lag. Various heat wave intensity measures are included as well, such as IntMn (mean intensity), IntMax (maximum intensity), and IntCum (cumulative intensity), alongside their absolute and relative threshold-based versions (IntMnabs, IntMaxabs, IntCumabs, IntMnrel, IntMaxrel, IntCumrel). Other features include the rates of onset and decline (Ronset and Rdecl), as well as the duration (Dur), which provides insights into the persistence of the conditions being measured. To improve model generalization across out-of-sample years and regions, temporal features and region labels were integrated into the modeling process to enhance the model's ability to capture dynamic trends and adapt to spatial variations in the data (Text S3). The detailed explanation of these features can be found in Text S4 of the Supporting Material. Our dataset consists of multiple short time series "clips" at each grid point, focusing on isolated extreme events during WHDW periods rather than continuous, long-term sequences. This is why we used XGBoost instead of temporal deep learning models like LSTM.

2.5.2. SHAP and SHAP interactions

To interpret the models and assess the contribution of each feature, we applied SHapley Additive exPlanations (SHAP), a technique grounded in cooperative game theory (Lundberg and Lee, 2017; Lundberg et al., 2019). SHAP assigns importance scores to variables using Shapley values. The SHAP value transparently quantifies per-variable contributions across individual forecasts, unlike partial R2's global variance explanation limited to linear models. By calculating SHAP values, we determined the primary influence of each feature on wind speed predictions. For a given instance x, the prediction of $f(x)$ can be decomposed as:

$$f(x) = \phi_0 + \sum_{i=1}^{M}\phi_i \tag{10}$$

where $f(x)$ denotes the prediction for input x. ϕ_0 denotes the average model output over the training data (baseline expectation). ϕ_i denotes the SHAP value for feature i, representing the contribution of feature iii to the deviation from the baseline.

The value ϕ_i is calculated as the Shapley value (Molnar, 2022):

$$\phi_i = \sum_{S\subseteq F\setminus\{i\}} \frac{|S|!(|F| - |S| - 1)!}{|F|!}\left[f_{S\cup\{i\}}(x_{S\cup\{i\}}) - f_S(x_S)\right] \tag{11}$$

where F denotes the set of all features. S a subset of features excluding i. $f_S(x_S)$ denotes the model output when only features in subset S are present. The expression inside the brackets is the marginal contribution of feature i.

To understand how pairs of features jointly influence the prediction (i.e., their interaction), SHAP interaction values ϕ_{ij} are computed:

$$f(x) = \phi_0 + \sum_{i=1}^{M}\phi_i + \sum_{i=1}^{M}\sum_{j>i}\phi_{ij} \tag{12}$$

where ϕ_{ij} measures the interaction effect between feature i and j beyond their individual contributions. When $i = j$, ϕ_{ii} includes both main and interaction effects of feature i with itself.

SHAP captures interactions between features, enabling a detailed examination of how variables collectively affect outcomes. This is especially useful for complex phenomena like temperature-wind speed relationships. It is important to emphasize that SHAP values represent feature-attribution scores, not statistical coefficients or direct physical causation. They quantify the marginal contribution of a feature to the model's prediction for each instance, conditional on interactions with other features, and provide both local (instance-level) and global (aggregated) interpretability. Combining SHAP with XGBoost addressed a common challenge in machine learning: the lack of interpretability in complex predictive models ("black boxes"). The integration of XGBoost and SHAP within the framework of explainable machine learning has been successfully applied across multidisciplinary research (Yan et al., 2025; Zhu et al., 2024).

2.6. Ecological impact assessment of WDHW events

Compound heat extremes such as WDHW can impose significant stress on ecosystems: elevated temperatures increase evapotranspiration and heat load, while stagnant wind conditions reduce convective cooling and intensify physiological drought stress. These conditions may lead to leaf overheating, stomatal closure, suppressed photosynthesis, and increased tree mortality (Barriopedro et al., 2023; Still et al., 2023).

To assess the ecological consequences of WDHW events, we conducted a spatial overlay analysis using global ecoregion, biomes and conservation priority data. We used the RESOLVE 2017 Ecoregions and Nature Needs Half (NNH) datasets (Dinerstein et al., 2017) to evaluate the spatial intersection between WDHW exposure and ecological conservation priorities. The RESOLVE dataset classifies the terrestrial surface into 867 terrestrial ecoregions, grouped into 14 biomes, and four NNH conservation categories based on current protection and remaining natural habitat: (1) Half Protected (HP): >50 % of the ecoregion is already protected; (2) Nature Could Reach Half Protected (NCRHP): <50 % protected, but sufficient remaining natural habitat exists to potentially reach 50 %; (3) Nature Could Recover (NCR): Combined protected and unprotected habitat is between 20–50 %, requiring restoration to achieve Half Protected; (4) Nature Imperiled (NI): ≤20 % of habitat remains; achieving Half Protected is not feasible in the short term, and urgent conservation is needed. Table 1 provides a summary of the NNH and biomes categories used in our analysis.

Table 1
The Nature Needs Half (NNH) and biomes categories used in our analysis.

Category	Name	Abbreviate
NNH	Half Protected	HP
	Nature Could Reach Half Protected	NCRHP
	Nature Could Recover	NCR
	Nature Imperiled	NI
BIOME	Temperate Grasslands, Savannas & Shrublands	TGS&S
	Temperate Broadleaf & Mixed Forests	TB&MF
	Temperate Conifer Forests	TCF
	Boreal Forests/Taiga	BFT
	Tundra	T
	Montane Grasslands & Shrublands	MG&S
	Flooded Grasslands & Savannas	FG&S
	Deserts & Xeric Shrublands	D&XS
	Tropical & Subtropical Coniferous Forests	T&SCF
	Tropical & Subtropical Moist Broadleaf Forests	T&SMBF
	Tropical & Subtropical Grasslands, Savannas & Shrublands	T&SGS&S
	Tropical & Subtropical Dry Broadleaf Forests	T&SDBF
	Mangroves	M

Each 0.25° grid cell was assigned both an ecoregion and a NNH conservation status. For each subcategory, we first calculated the mean event frequency of the grid cells within it, which represents the frequency level of WDHW events in that category. In addition, the grid cells within each category were grouped into frequency bins based on their event frequencies. The frequency distribution was then computed and normalized by the total number of grid cells in each category to ensure comparability across different categories. This approach allowed us to identify patterns and assess whether certain ecological regions are more prone to WDHW events than others.

3. Results

3.1. Wind power availability and seasonal variations

The spatial distribution of average wind power density (WPD) and its monthly variations across seven major geographical power regions in China are shown in Fig. 2, which align with common divisions used in China's wind energy assessments. China shows significant geographical differences in wind energy resources, with averaged WPD ranging from 3.3 W m^{-2} to 617.3 W m^{-2}, a difference exceeding 187 times. The high-WPD areas, defined as those at or above the 70th percentile, cover approximately 30 % of the national territory and are concentrated primarily in the northern Qinghai-Tibet Plateau and northern Inner Mongolia Plateau. In contrast, low-WPD restricted areas like the western Yunnan-Guizhou Plateau and Sichuan Basin have WPD below 25.4 W m^{-2}. The color gradient corresponds to percentile rankings, also showing a steep resource gradient in high-value areas. From the highest percentile to the 80th percentile, the WPD dropping by 72.8 % (617.3 W m^{-2} to 167.6 W m^{-2}), while from the 80th to the 0th percentile, WPD values follow a smoother and less steep decrease, indicating a highly concentrated wind resources gradient. Further examination indicates that there are not significant interannual variability in the spatial patterns of WPD, although there is an increase in WPD in some of the western and northern regions in the past decade (Fig. S4).

The radar charts in Fig. 2 represents monthly mean wind power density values in different power regions, indicating a significant regional and seasonal variability where northern and high-altitude areas typically show stronger wind resources compared to southern and coastal zones. The WPD generally peak in early spring, from February in southern regions (South, Tibet) to April for Northern regions (Northeast, Northwest, North), and being lowest in late summer (August–October). The nation averages shows that the monthly mean wind power density peaks at 141.34 W/m^2 in April and reaches its lowest at 74.46 W/m^2 in August. However, regions like Tibet displays greater variability across months, with differences between peak and low values often exceeding 100 W/m^2 (280.90 W/m^2 in February to 119.78 W/m^2 in August). In contrast, low-potential regions like South observes monthly differences typically under 30 W/m^2, indicating more stable but weaker wind conditions. Further analysis of the interannual variability in seasonal WPD for various periods (Fig. S5) shows no marked annual changes and the seasonal patterns remain consistent with those observed in radar charts in Fig. 2.

3.2. Spatiotemporal evolution of compound wind droughts and heat waves (WDHW) events

Fig. 3a shows spatial variations in the frequency of compound WDHW events from 2000 to 2022. Detailed spatial and temporal trend maps for individual WD and HW events can be found in Text S5 and Fig. S6 in the Supporting Material. High-frequency areas of WDHW events, where the cumulative frequency exceed 70 days are primarily

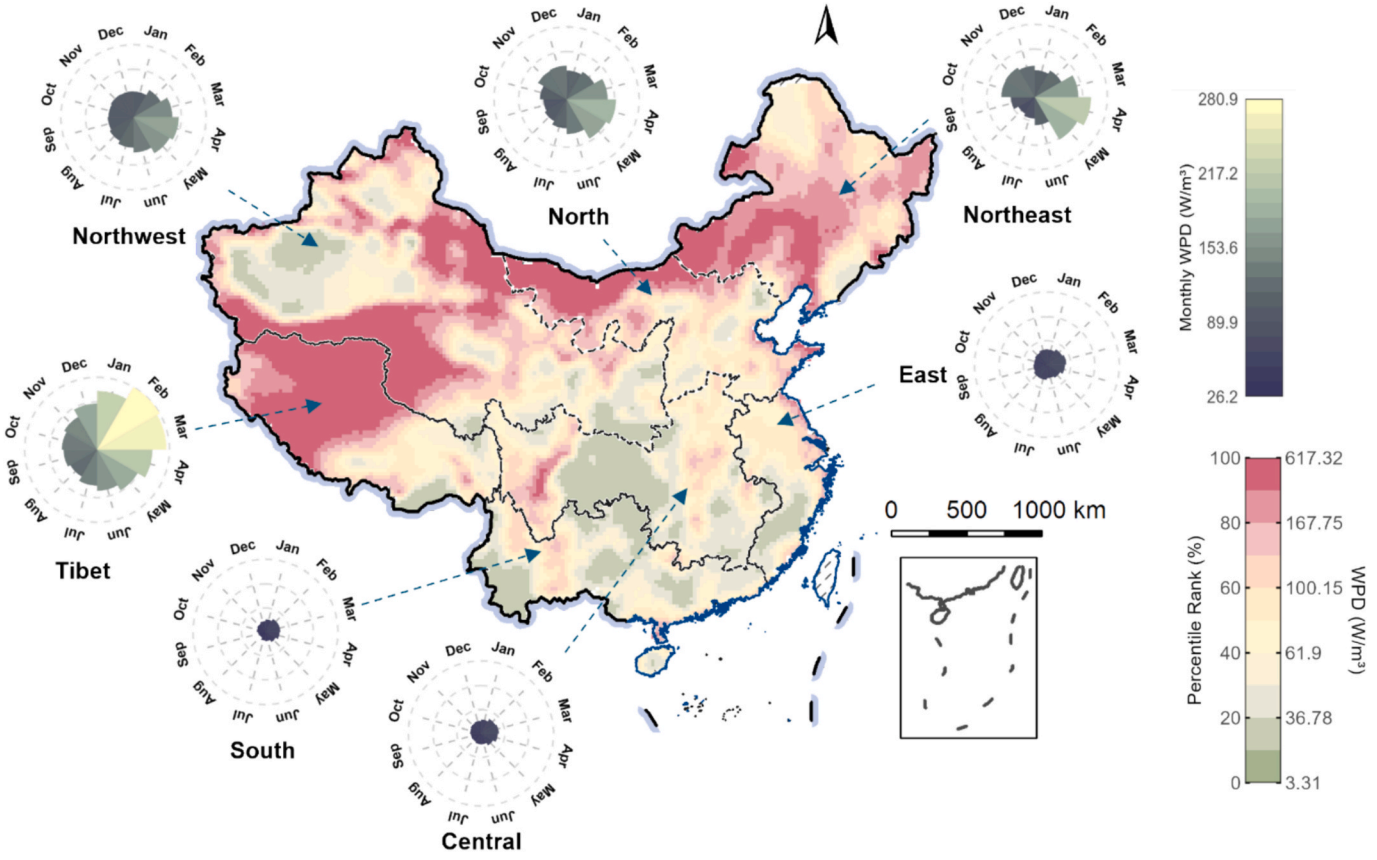

Fig. 2. Spatial pattern of wind power density (WPD) and its seasonal variations in mainland China during 2000–2022. It represents the long-term average WPD across 2000–2022, calculated as the mean of 23-year annual means.

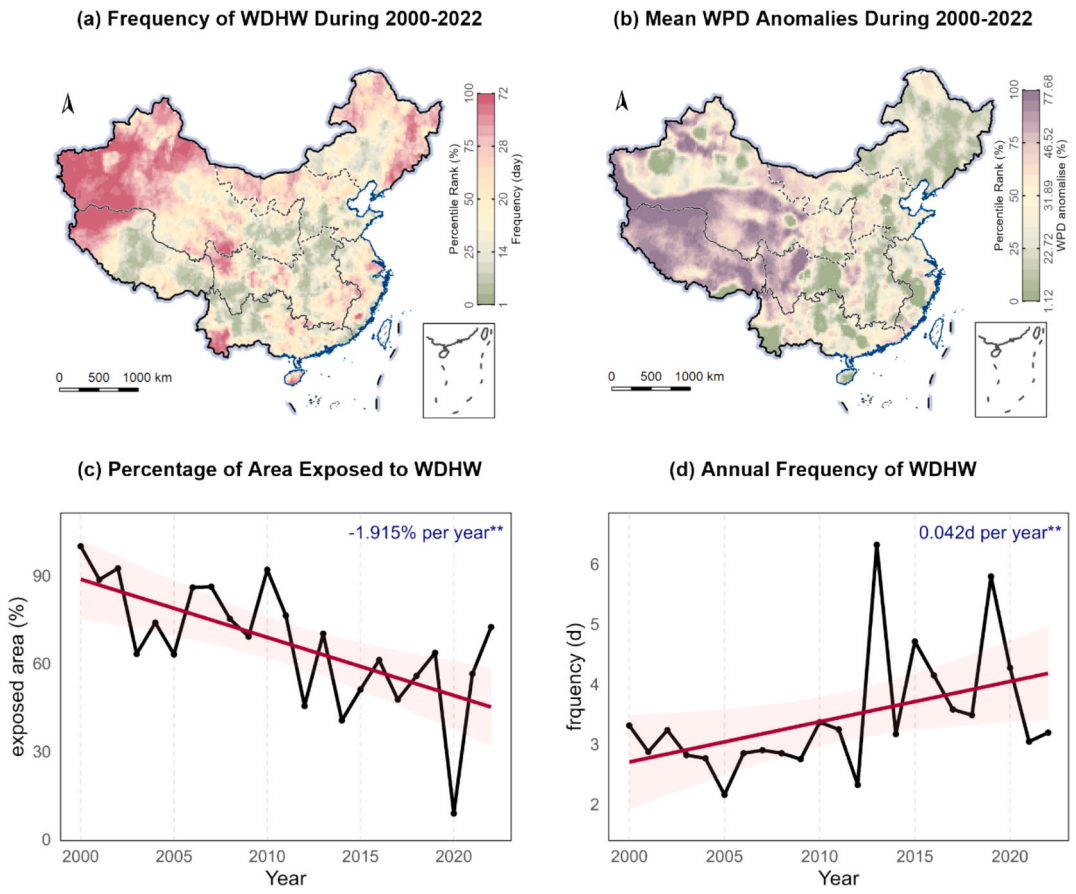

Fig. 3. Spatial-temporal changes of frequency, trend and annual variation of compound wind droughts and heat waves (WDHW) events from 2000 to 2022. (**a**) Cumulative number of days experiencing compound wind droughts and heat waves (WDHW) events over the entire study period; (**b**) Mean wind power density (WPD) anomalies during WDHW compared to its climatological mean; (**c**) The percentage of area exposing at last one compound WDHW event of the year; (**d**) The average annual frequency in areas experiencing compound WDHW events.

located in northwestern China. Some parts of the northeast, central and south regions also exhibit relatively high frequencies, ranging from 30 to 70 days. In contrast, most of northern and central China, are less prone to the simultaneous occurrence of wind power deficiencies and heat waves, with an annual frequency of less than one day per year. To further identify regions with statistically significant concentrations of compound WDHW events, we applied the Getis-Ord Gi* spatial clustering statistic (Text S6) (Getis and Ord, 1992). This analysis revealed the spatial pattern of WDHW hotspots (Fig. S7) are consistently to Fig. 3a, where high-frequency clusters are statistically significant.

Fig. 3b shows the mean WPD anomalies during the compound WDHW events compared to its climatological mean. The highest WPD anomalies are concentrated in the Northwest and Tibet regions, with anomalies falling in the 75th to 100th percentile (approximately 46.52 to 77.68 W/m^2). This pattern aligns with regions known for higher WPD, suggesting that areas with typically strong winds experience more substantial declines during heat wave conditions. Conversely, the cumulative WPD anomalies in South, Central and Northeast regions are less pronounced due to their limited wind power potential, even though some parts regions experience relatively frequent occurrences of compound WDHW events (Fig. 3a).

Regarding annual time series, a declining trend in the percentage of the research area experiencing at least one compound WDHW event is observed (Fig. 3c). This trend decreases at a rate of 1.915 % per year, suggesting fewer regions are impacted over time. However, Fig. 3d indicates that in areas still affected, the average annual frequency of events increased by 0.042 d yr^{-1}. This modest increase indicates more frequent compound WDHW events in these regions.

3.3. XGBoost-SHAP modeling results for WDHW events

Fig. 4 shows the performance evaluation of four XGBoost models designed to predict 100-m hub heights wind speed during WHDW periods. The scatter plots comparing observed and predicted wind speeds for the training, cross-validation, and test datasets. Overall, the XGBoost model performed well across all datasets, with slight variations in accuracy. In the training dataset (Fig. 4a), the model demonstrated strong predictive accuracy, with a R^2 of 0.88 and a RMSE of 0.70 m/s. The red line, representing the regression line, closely follows the ideal 1:1 line (black dashed line), indicating a high correlation between observed and predicted wind speeds. For the cross-validation dataset (Fig. 4b), the model's performance remained robust, with an R2 of 0.83 and an RMSE of 0.84 m/s. In the test dataset (Fig. 4c), the model maintained reasonable predictive accuracy, yielding an R2 of 0.84 and an RMSE of 0.83 m/s. The correlation between observed and predicted wind speeds in the test set further supports the generalizability and robustness of the XGBoost model.

Fig. 5 shows the feature importance in an XGBoost model designed to predict 100 m wind speed during WDHW periods, utilizing SHAP values to quantify the contribution of each feature. The SHAP values illustrate how changes in independent feature variables influence individual XGBoost model predictions. As shown in Fig. 5a, Tmax (maximum temperature) is the most important feature, with the highest average SHAP value of 0.722, followed closely by VPD (vapor pressure deficit) and IntMnabs (mean heat wave intensity) with relatively high SHAP values of 0.698 and 0.615. Other highly influential features include Year, IntMaxabs (maximum heat wave intensity) and TmaxL1

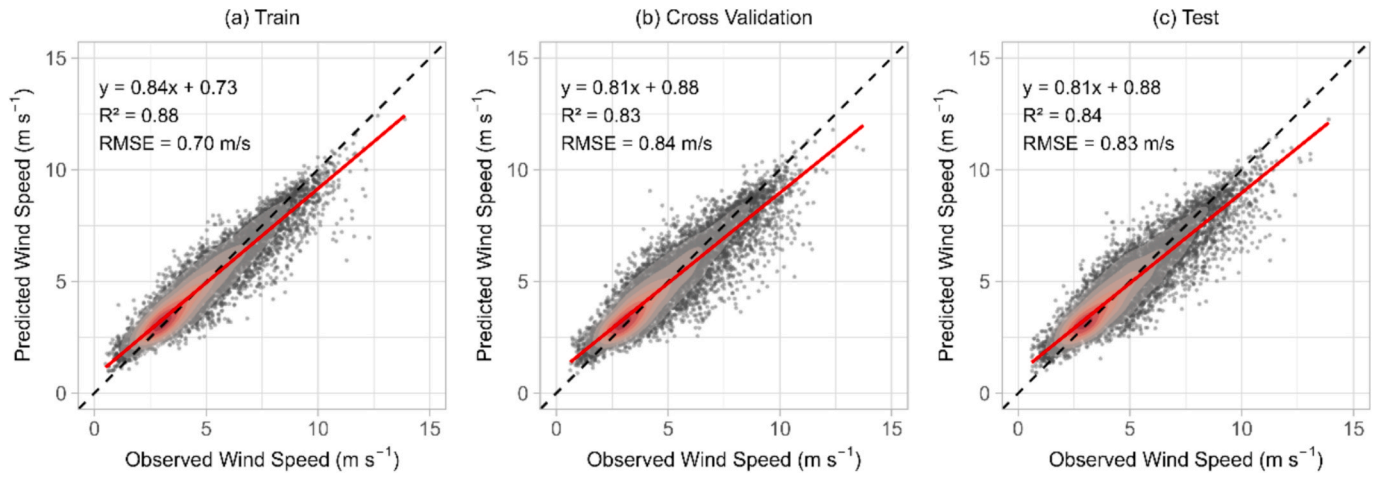

Fig. 4. Scatter plots comparing observed and predicted wind speeds (m s^{-1}) in the XGBoost model for the training (a), cross-validation (b), and test (c) datasets.

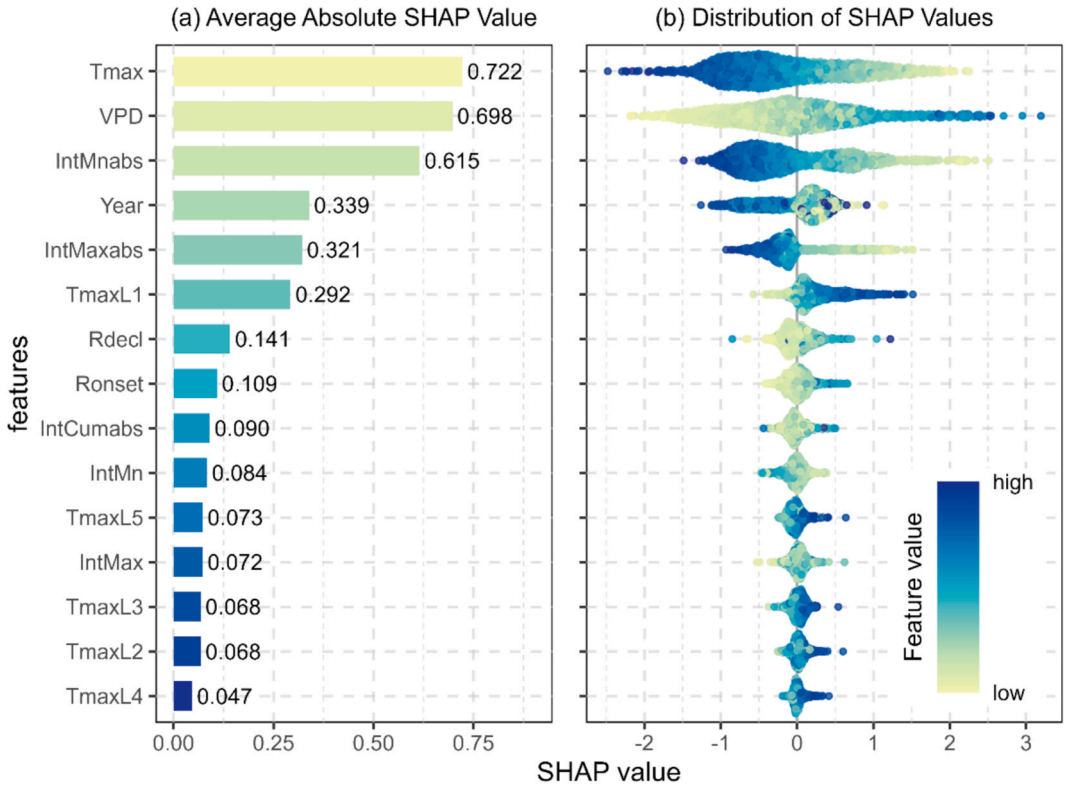

Fig. 5. Feature importance analysis based on SHAP (SHapley Additive exPlanations) values. **(a)** Bar chart displaying the mean absolute SHAP values for each feature, ranked by their contribution to the XGBoost model's predictions. **(b)** Summary plot illustrating the distribution of SHAP values across individual samples for each feature, with colors indicating feature values from low (dark blue) to high (light yellow). Features include Tmax (maximum temperature), VPD (vapor pressure deficit), IntMnabs (heat wave mean intensity), Year, IntMaxabs (heat wave maximum intensity), Rdel (heat wave decline rate), Ronset (heat wave onset rate), IntCumabs (cumulative heat wave intensity), IntMn (heat wave mean intensity), TmaxL5 (Tmax lagged by 5 days), and TmaxL1-L5 (Tmax lagged by 1–5 days). (For interpretation of the references to color in this figure legend, the reader is referred to the web version of this article.)

(maximum temperature lagged by 1 day), with SHAP values of 0.339, 0.321 and 0.292, respectively. Features like Rdel (heat wave decline rate), Ronset (heat wave onset rate) and other factors have a less impact, with SHAP values ranging from 0.047 to 0.141. Fig. 5b further reveals that Tmax and VPD, the second most influential environmental variables, exhibit a wide spread of SHAP values, ranging from −3 to 3, indicating a significant and varying impact on the model's output depending on their respective feature values.

Fig. 6 presents the SHAP interaction values, which capture the interactive effects among features in an XGBoost model used to predict 100 m wind speed during WDHW periods. The heatmap visually represents the strength of these pairwise interactions. The most substantial interaction is observed between Tmax and TmaxL1, with a SHAP value of 0.420, indicating current maximum temperature and the previous day's temperature jointly shape wind speed during WDHW periods. The subsequent strongest interactions occur between Tmax and VPD, with a SHAP value of 0.321, and between VPD and IntMaxabs, with a SHAP value of 0.314. These interactions indicate that the combined effects of moisture and temperature-related heat wave intensity conditions significantly impact wind speed during WDHW periods. On the other

Fig. 6. Heatmap of SHAP interaction values illustrating the interactive effects between feature pairs in an XGBoost model for wind speed prediction. The diagonal elements represent self-interactions, indicating each feature's individual variability, while off-diagonal elements show the strength of interactions between different features. Features include Tmax (maximum temperature), VPD (vapor pressure deficit), IntMnabs (mean heat wave intensity), Year, IntMaxabs (heat wave maximum intensity), Rdel (heat wave decline rate), Ronset (heat wave onset rate).

hand, features like Ronset (heat wave onset rate) and Rdel (heat wave decline rate) show weaker interactions with other features, with average interaction values below 0.05, indicating that their combined influence on wind speed is less significant.

To explore the interactions between key meteorological features and their influence on predicted 100 m wind speeds during WDHW periods, we computed SHAP interaction values and visualized them in dependence plots (Fig. 7). In Fig. 7a, the SHAP values for Tmax exhibit a pronounced negative trend, declining from approximately 2 at low Tmax (~10 °C) to −2 at high Tmax (~40 °C), indicating that elevated maximum temperatures strongly suppress predicted wind speeds. Colored by VPD (yellow for low, blue for high), the plot shows that high VPD exacerbates this suppression at Tmax > 30 °C, where blue points cluster at more negative SHAP values. Fig. 7b shows the main effect of VPD on SHAP, rising from −2 at ~ 1 kPa to 2 at ~ 4 kPa. Coloring by Tmax reveals an interaction where high Tmax (blue) shifts the curve downward at elevated VPD. Fig. 7c is the main effect of IntMnabs, displaying patterns similar to those observed for Tmax in Fig. 7a. In Fig. 7d, the SHAP values increased mildly from 0 to + 2 as TmaxL1 rises, colored by current Tmax. In Fig. 7e and 7f, the SHAP values of heat wave decline and onset rates (Rdecl, Ronset) displays a non-linear, inverted-U pattern, which are not directly correlated with changes in Tmax.

3.4. Ecological impact and implication of WDHW events

To explore the ecological dimensions of WDHW events, we analyzed the frequency and distribution of the events within different ecoregion classifications. Fig. 8 shows the frequency of WDHW events across different ecological and conservation status areas based on the NNH conservation categories and biome categories, providing insights for wind farm development decisions that ensure sustainable energy production while minimizing the environmental costs of wind energy generation.

As shown in Fig. 8a, the frequency of WDHW events reveals significant differences across these conservation categories. The Half Protected (HP) areas have the highest frequency of compound WDHW events, with a value of 28.80 days. These regions, where more than 50 % of the habitat is protected, are more severely affected by the negative impacts of low wind and heat wave events on wind power generation. Additionally, these areas are typically ecologically sensitive, with unique species and fragile habitats that may be further threatened by wind farm development. On the other hand, the Nature Imperiled (NI)

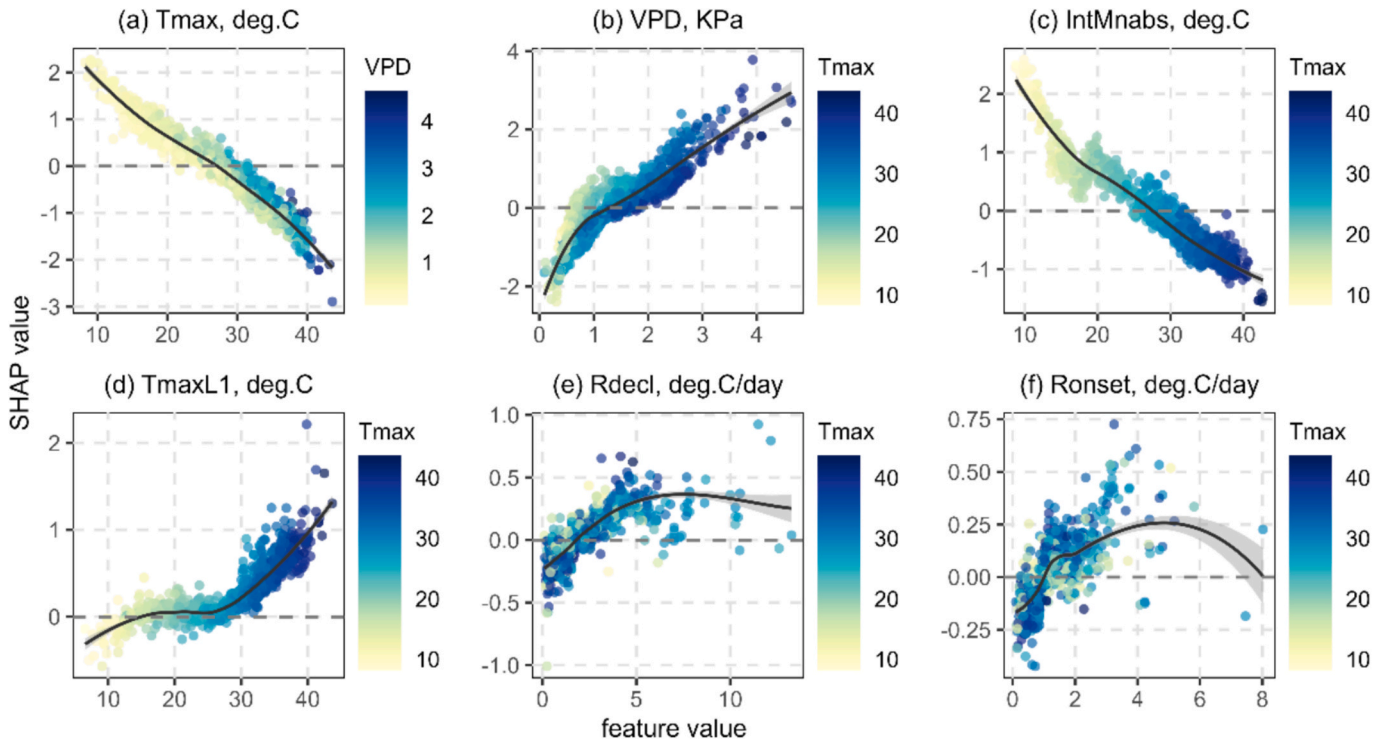

Fig. 7. SHAP interaction plots of key features in wind speed predictions during WDHW period. (a) Tmax (maximum temperature); (b) VPD (vapor pressure deficit), colored by Tmax; (c) IntMaxabs (heat wave maximum intensity); (d) TmaxL1 (one-day lagged Tmax); (e) Rdecl (rate of heat wave decline); (f) Ronset (rate of heat wave onset). Plot a is colored by VPD, while plots b-f are colored by Tmax.

category has the lowest frequency of WDHW events at 16.35 days, representing regions with less than 20 % protected habitat and severe habitat fragmentation. Although these areas experience fewer compound WDHW events, they are often ecologically degraded and face significant land-use conflicts from urbanization and agriculture. In contrast, the Nature Could Reach Half Protected (NCRHP) and Nature Could Recover (NCR) areas offer a balance between wind energy potential and conservation opportunities. These categories experience slightly lower frequencies of compound events, with values of 23.73 days and 22.31 days, respectively.

Regarding the WDHW event frequency across different types of biomes (Fig. 8c), results reveals that the Deserts & Xeric Shrublands (D&XS) shows the highest frequency of compound events (28.75 days). This is likely due to the extreme climate conditions in desert regions, where high temperatures combined with low wind conditions might be more frequent. These areas are likely already prone to extreme temperatures and low precipitation. When coupled with extreme heat, the impacts could be more severe, exacerbating conditions like soil degradation, water scarcity, and stress on local flora and fauna. Montane Grasslands & Shrublands (MG&S) and Flooded Grasslands & Savannas (FG&S) biomes also have relatively high frequencies (24.72 days and 23.12 days). Temperate Grasslands, Savannas & Shrublands (TGS&S) biome has a moderate frequency at 19.27 days. These areas area widely distributed in the Northwestern of mainland China, likely experiencing strong seasonal variations, including extreme weather events. Temperate Conifer Forests (TCF) and Temperate Broadleaf & Mixed Forests (TB&MF) are biomes have relatively lower frequencies (18.27 days and 18.46 days), respectively. The Tropical & Subtropical Moist Broadleaf Forests (T&SMBF) biome has the lowest frequency of these events (16.98 days). These regions, being more temperate or tropical, may have more buffering capacity against extreme conditions due to higher vegetation cover, greater moisture availability, and more robust ecosystems. The histograms in Fig. 8b and 8d show the frequency distribution of WDHW events across various ecological and biome categories. These patterns are consistent with the maps in Fig. 8a and 8c, revealing how WDHW event frequency differs by conservation status and biomes.

4. Discussion

4.1. Comparison with previous studies, alternative data and approaches

This study provides a spatially and temporally resolved assessment of how compound wind drought and heat waves threaten wind energy reliability across China. Consistent with previous work (CMA Wind and Solar Energy Resources Centre, 2024; Sun et al., 2024), we confirm strong regional disparities in WPD, with persistently high-WPD zones in northern and northwestern regions and low-WPD areas in the southwest. Seasonal declines in WPD during summer, especially in North and Northeast China, coincide with peak electricity demand, presenting a critical challenge for energy security (Sun et al., 2024; Zhuo et al., 2022).

WDHW events present a compound risk by aligning low wind output with surging cooling demand, as exemplified by the July 2021 event in northeastern China, where turbine output fell below 0.1 % of installed capacity (Power Sector Roundtable, 2023). Topography plays a significant role in WDHW distribution, with low-lying areas like the Sichuan Basin trapping heat and stifling winds, while high-elevation regions like the Tibetan Plateau experience fewer compound events due to cooler temperatures and stronger winds (Wu et al., 2018; Zhou et al., 2023). To further evaluate the robustness of the identified trends, we compared the CN05.1 dataset with ERA5 reanalysis data. As shown in Fig. S8 and Text S7, the ERA5 dataset generally exhibits a consistent pattern with the CN05.1 dataset, although notable differences are observed in regions such as Tibet and the southern areas (Minola et al., 2024). These discrepancies are primarily attributed to variations in wind speed between the two datasets. Nonetheless, both datasets confirm a significant increase in the frequency of WHDW over the past two decades, thereby reinforcing the robustness of the observed upward trends.

Our choice of XGBoost over other temporal deep learning models is

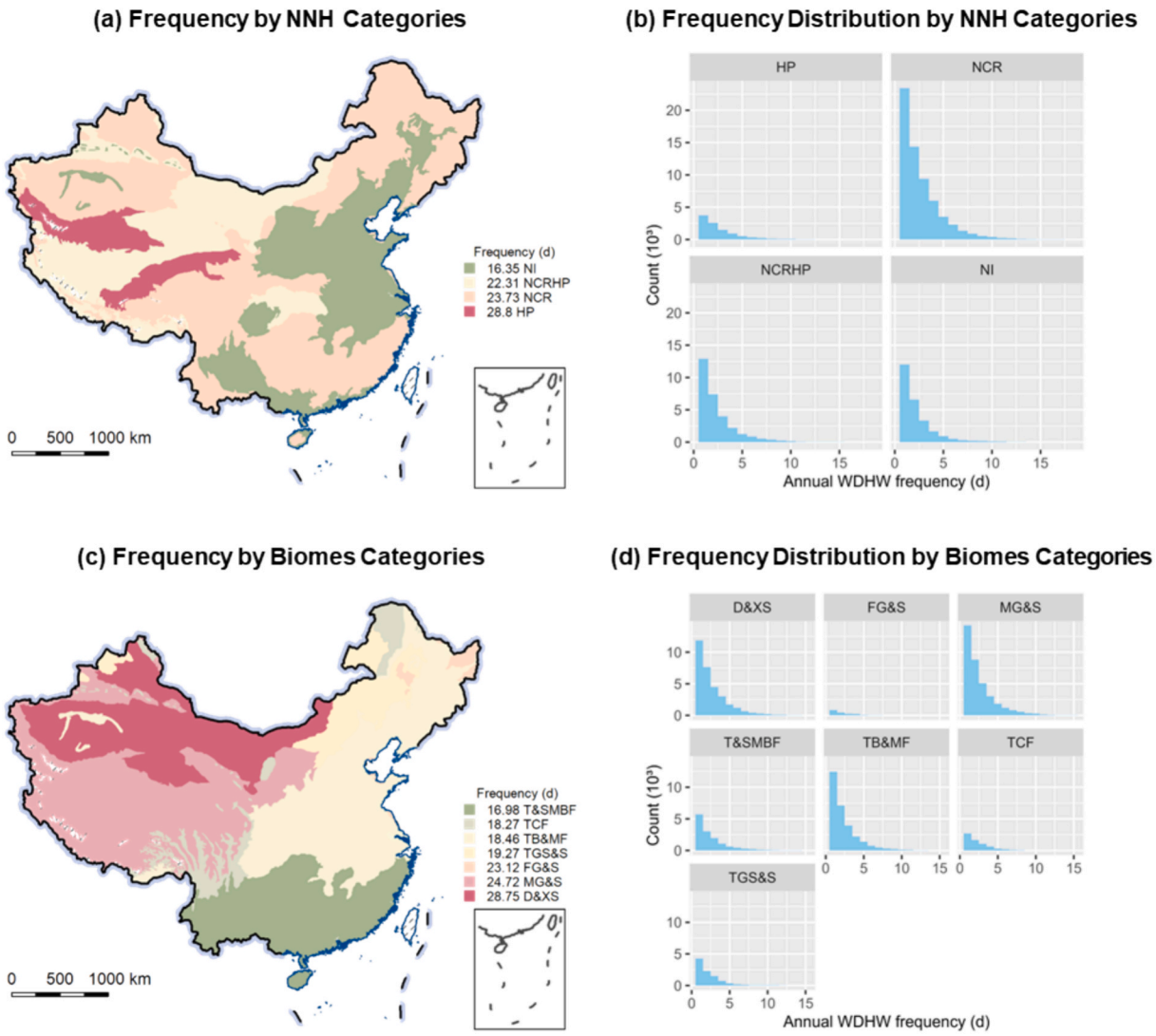

Fig. 8. The frequency and distribution of WDHW events of four Nature Needs Half (NNH) ecoregions. The NNH conservation categories are based on current protection and remaining natural habitat: Half Protected (HP), Nature Could Reach Half Protected (NCRHP), Nature Could Recover (NCR) and Nature Imperiled (NI). (a) and (c) show the spatial distributions of WDHW events in different NNH ecoregions (a) and biomes (c), respectively. (b) and (d) display the frequency distributions across the different NNH ecoregions (b) and biomes (d), respectively.

based on the specific nature of the dataset, which focuses on extreme events characterized by short-duration bursts rather than long-term trends. Additionally, we conducted a comparison between XGBoost and Random Forest (RF) as part of our evaluation of alternative approaches. Fig. S9 shows the performance of RF model on the training dataset, cross-validation and test datasets. The XGBoost model outperformed the RF model, achieving R^2 values of 0.88, 0.83, and 0.84 for the training, cross-validation, and test datasets, respectively, compared to 0.67, 0.66, and 0.66 for the RF model. These findings suggest that XGBoost offers superior fitting accuracy, validation performance, and generalizability in our study compared to the RF model.

The XGBoost-SHAP framework elucidates the importance of Tmax and VPD in shaping wind speed at turbine hub heights during WDHW periods. Tmax's leading SHAP value reflects its central role in boundary-layer dynamics: extreme heat increases sensible heat fluxes, suppressing convective mixing and thus near-surface winds (Miralles et al., 2019). This aligns with the findings that persistent high-pressure systems during heat waves reduce wind speeds by enhancing atmospheric stability and air mass stagnation (Horton et al., 2012; Nabizadeh et al., 2019). Spatially, these negative correlations between Tmax and wind speed are predominantly concentrated in southwestern China, especially within the Tibetan Plateau and adjacent areas (Fig. S10), where topographic complexity amplifies boundary-layer effects and limits turbulent mixing, potentially leading to prolonged wind lulls during WDHW events. The integration of VPD as the second-most important feature further illuminates these processes, as high VPD, often amplified by Tmax, triggers ecophysiological responses like stomatal closure in vegetation, reducing latent heat release and stabilizing the boundary layer (Novick et al., 2016). In isolation, VPD exhibits a positive main effect on SHAP values, with VPD and wind speed show positive correlations across most regions (Fig. S11). However, the Tmax-VPD interaction modifies this, with high VPD exacerbates 100 m wind speed suppression at Tmax $>$ 30 °C, exemplifying hot-drought feedbacks where compound extremes limit evapotranspiration and reinforce atmospheric stillness (Anderegg et al., 2020).

4.2. Policy implications

Collectively, our findings highlight the convergence of rising heat wave frequency, declining wind speeds during extreme heat, and increasing electricity demand poses a challenge to energy sustainability in China. Wind power, while a cornerstone of renewable energy

expansion, is inherently vulnerable to climate-driven disruptions, particularly during summer months when energy demand peaks and wind power supply often decreases. The vulnerability of wind energy to compound wind droughts and heat waves necessitates a diversified renewable energy portfolio.

The spatial heterogeneity of compound wind droughts and heat waves events also demands region-specific energy strategies. In vulnerable regions, such as south-central and southeastern China, facing frequent disruptions, policies could prioritize backup systems and demand response programs to manage peak loads. Conversely, in less-affected areas like the northwest, where wind power remains stable year-round, policymakers could expand wind capacity with confidence, optimizing resource allocation. Regional grid interconnections should also be strengthened to allow power transfers from low-risk to high-risk zones during extreme events, enhancing overall system resilience.

As heat waves are projected to intensify under climate change, wind energy infrastructure should be adapted to withstand extreme conditions. Current turbine designs, optimized for average wind speeds, may underperform during prolonged low-wind periods. Stakeholders can incentivize the development and deployment of low-wind-speed turbines and incorporate cooling systems to maintain turbine efficiency during high temperatures. Additionally, upgrading transmission lines to reduce heat-related efficiency losses, especially during heat waves, will ensure that generated power reaches consumers effectively. Overall, this research highlights the necessity of comprehensive preparedness frameworks to account for compound event risks under a warming climate.

We highlight multi-source energy integration strategies enhance grid resilience under compound extreme events by leveraging complementary generation patterns across renewables. For instance, solar energy may peak during heat waves due to clear skies and high irradiance, acting as a natural hedge against wind droughts. To quantify this dynamic, we analyzed anomalies in solar photovoltaic power density as a proxy for solar resource availability during WDHW periods (see details in Text S8). As shown in Fig. S12, central and northwestern China, specifically Shanxi, Shaanxi, and Ningxia provinces, exhibited increased solar potential during WDHW events. This indicates a potential complementarity between solar and wind energy during extreme events. On the other hand, hydropower faces compounded stress during concurrent heat-drought events due to reduced river flow and increased evaporation. Yet, its storage capacity provides flexibility to balance intermittent solar and wind generation (Wang et al., 2021). Hybrid wind-solar-hydropower systems thus create a resilience triad: solar buffers wind deficits, hydropower storage smooths intra-day variability, and cross-regional transmission redistributes surpluses from solar-gain regions (e.g., Ningxia) to hydropower-dependent basins (e.g., Sichuan) during deficits.

The ecological impact analysis of WDHW events identified ecoregions that face dual vulnerability: ecological sensitivity and frequent compound climate extremes. The results highlight regions where wind energy development should be carefully managed to avoid exacerbating biodiversity threats. The Half Protected areas should be avoided for wind farm development due to their ecological sensitivity and high frequency of compound WDHW events. The Nature Imperiled category areas experience fewer compound WDHW events and are often ecologically degraded and face significant land-use conflicts from urbanization and agriculture. The development of wind farms in these areas could exacerbate these issues further. In contrast, developing wind farms in the Nature Could Recover and Nature Could Reach Half areas could bring dual benefits, as they would not only promote renewable energy generation but also support restoration efforts. Given the moderate frequency of WDHW events in these areas, wind farms are feasible, provided they are carefully sited and designed to minimize environmental degradation. Additionally, developers could integrate conservation efforts with wind farm projects, enhancing the ecological resilience of these areas while providing clean energy.

4.3. Limitations and future directions

While this study sheds light on the compound effects of wind-resource droughts and heat waves in China, it also highlights several areas for deeper exploration. First, the study is based on gridded data at a $0.25^\circ \times 0.25^\circ$ spatial resolution, which corresponds to approximately 27 km × 27 km at mid-latitudes. While this resolution provides robust regional estimates, it may not fully capture localized wind patterns and microclimatic variability, particularly in complex terrain or urbanized regions, due to spatial averaging and the coarse representation of fine-scale atmospheric and surface processes (Karger et al., 2023). Similarly, the 23-year study period (2000–2022) offers substantial insights but may not fully reflect longer-term trends or decadal variability. Future research could employ higher-resolution and extended datasets to improve the granularity of the analyses. Second, the XGBoost and SHAP framework provides a powerful and interpretable approach to modeling wind speed variability, yet physical-informed challenges remain. Future studies could explore hybrid models combining physical principles with machine learning to boost interpretability or test the current framework's generalizability in other wind-reliant regions. Additionally, the analysis focuses on temperature-related drivers, but other factors, such as atmospheric pressure patterns, humidity, land use changes, or urbanization, may also influence wind speed and compound events.

Finally, while our study focuses on the observation-based historical identification, future work could integrate CMIP6-based future projections under IPCC SSP scenarios to bridge historical patterns with plausible climate trajectories. Under both SSP2-4.5 (intermediate emissions) and SSP5-8.5 (high emissions), models from CMIP6 and related assessments project a substantial rise in heat wave frequency, duration, and intensity across East Asia and China (Speizer et al., 2022). Concurrently, under the higher-emission SSP5-8.5 pathway, China is projected to experience a continued decline in near-surface wind speeds (Long et al., 2021). The combined effect may translate into a higher probability and severity of compound wind droughts and heat waves in the future under high-emission scenarios.

5. Conclusions

This study establishes WDHW as critical environmental indicators for monitoring climate-driven stress on energy and ecological systems in China from 2000 to 2022, using observational data and interpretable machine learning (XGBoost and SHAP). Our findings highlight the spatial heterogeneity of WDHW events, with higher frequencies observed in northwestern China, and an overall increase in event frequency in affected regions. The XGBoost model demonstrated strong predictive performance, underscoring the robustness of the analysis. Key drivers, identified through SHAP analysis, include Tmax and VPD, with their interaction showing how heat and dryness significantly suppress wind speed at 100-m hub heights. Ecological analysis reveals that regions with higher WDHW frequencies, such as Half Protected ecoregions and Deserts & Xeric Shrublands biomes, face dual vulnerabilities to biodiversity and energy systems. The study underscores the need for integrated approaches to address the compounded risks of climate extremes and enhance resilience in both ecological and energy systems.

CRediT authorship contribution statement

Jiewen You: Writing – original draft, Methodology, Investigation, Formal analysis, Data curation, Conceptualization. **Fangxu Yin:** Writing – review & editing, Visualization, Software, Methodology. **Boen Zhang:** Writing – review & editing, Resources. **Mo Zhou:** Writing – review & editing, Validation. **Yamin Qing:** Writing – review & editing, Resources. **Ying Chen:** Writing – review & editing, Project administration. **Lu Gao:** Writing – review & editing, Supervision, Project administration, Funding acquisition.

Declaration of competing interest

The authors declare that they have no known competing financial interests or personal relationships that could have appeared to influence the work reported in this paper.

Acknowledgments

The study was supported by the National Natural Science Foundation of China (42271030), Fujian Provincial Funds for Distinguished Young Scientists (2022 J06018), Natural Science Foundation of Fujian Province (2022 J01604) and Foundation for Cultivated Young Talents of Fujian Province, China (2025350408).

Appendix A. Supplementary data

Supplementary data to this article can be found online at https://doi.org/10.1016/j.ecolind.2025.114114.

Data availability

The processed data and main codes are publicly available at the following Zenedo link: https://zenodo.org/records/16793478. Any other data will be made available on request.

References

Anderegg, W.R.L., Trugman, A.T., Badgley, G., Konings, A.G., Shaw, J., 2020. Divergent forest sensitivity to repeated extreme droughts. Nat. Clim. Chang. 10, 1091–1095. https://doi.org/10.1038/s41558-020-00919-1.

Antonini, E.G.A., Virgüez, E., Ashfaq, S., Duan, L., Ruggles, T.H., Caldeira, K., 2024. Identification of reliable locations for wind power generation through a global analysis of wind droughts. Commun. Earth Environ. 5, 103. https://doi.org/10.1038/s43247-024-01260-7.

Barriopedro, D., García-Herrera, R., Ordóñez, C., Miralles, D.G., Salcedo-Sanz, S., 2023. Heat waves: physical understanding and scientific challenges. Rev. Geophys. 61, e2022RG000780. https://doi.org/10.1029/2022RG000780.

Bentéjac, C., Csörgő, A., Martínez-Muñoz, G., 2019. A Comparative Analysis of XGBoost. https://doi.org/10.1007/s10462-020-09896-5.

Bloomfield, H.C., Suitters, C.C., Drew, D.R., 2020. Meteorological drivers of European power system stress. J. Renewable Energy 2020, 5481010. https://doi.org/10.1155/2020/5481010.

Chen, T., Guestrin, C., 2016. XGBoost: a scalable tree boosting system, in. In: Proceedings of the 22nd ACM SIGKDD International Conference on Knowledge Discovery and Data Mining, pp. 785–794. https://doi.org/10.1145/2939672.2939785.

CMA Wind and Solar Energy Resources Centre, 2024. China Wind and Solar Energy Resources Bulletin.

Davis, S.J., Lewis, N.S., Shaner, M., Aggarwal, S., Arent, D., Azevedo, I.L., Benson, S.M., Bradley, T., Brouwer, J., Chiang, Y.-M., Clack, C.T.M., Cohen, A., Doig, S., Edmonds, J., Fennell, P., Field, C.B., Hannegan, B., Hodge, B.-M., Hoffert, M.I., Ingersoll, E., Jaramillo, P., Lackner, K.S., Mach, K.J., Mastrandrea, M., Ogden, J., Peterson, P.F., Sanchez, D.L., Sperling, D., Stagner, J., Trancik, J.E., Yang, C.-J., Caldeira, K., 2018. Net-zero emissions energy systems. Science 360, eaas9793. https://doi.org/10.1126/science.aas9793.

Dinerstein, E., Olson, D., Joshi, A., Vynne, C., Burgess, N.D., Wikramanayake, E., Hahn, N., Palminteri, S., Hedao, P., Noss, R., Hansen, M., Locke, H., Ellis, E.C., Jones, B., Barber, C.V., Hayes, R., Kormos, C., Martin, V., Crist, E., Sechrest, W., Price, L., Baillie, J.E.M., Weeden, D., Suckling, K., Davis, C., Sizer, N., Moore, R., Thau, D., Birch, T., Potapov, P., Turubanova, S., Tyukavina, A., de Souza, N., Pintea, L., Brito, J.C., Llewellyn, O.A., Miller, A.G., Patzelt, A., Ghazanfar, S.A., Timberlake, J., Klöser, H., Shennan-Farpón, Y., Kindt, R., Lillesø, J.-P.-B., van Breugel, P., Graudal, L., Voge, M., Al-Shammari, K.F., Saleem, M., 2017. An ecoregion-based approach to protecting half the terrestrial realm. Bioscience 67, 534–545. https://doi.org/10.1093/biosci/bix014.

ECMWF, 2021. European Centre for Medium-Range Weather Forecasts (ECMWF). Low winds. https://climate.copernicus.eu/esotc/2021/low-winds.

Getis, A., Ord, J.K., 1992. The analysis of spatial association by use of distance statistics. Geogr. Anal. 24.

Gilbert, R.O., 1987. "6.5 Sen's Nonparametric Estimator of Slope", Statistical methods for environmental pollution monitoring. John Wiley & Sons.

Graczyk, D., Pińskwar, I., Choryński, A., Stasik, R., 2024. Less power when more is needed. Climate-related current and possible future problems of the wind energy sector in Poland. Renew. Energ. 232, 121093. https://doi.org/10.1016/j.renene.2024.121093.

Grams, C.M., Beerli, R., Pfenninger, S., Staffell, I., Wernli, H., 2017. Balancing Europe's wind-power output through spatial deployment informed by weather regimes. Nat. Clim. Chang. 7, 557–562. https://doi.org/10.1038/nclimate3338.

Horton, D.E., Harshvardhan, Diffenbaugh, N.S., 2012. Response of air stagnation frequency to anthropogenically enhanced radiative forcing. Environ. Res. Lett. 7, 44034. doi:10.1088/1748-9326/7/4/044034.

Hultgren, A., Carleton, T., Delgado, M., Gergel, D.R., Greenstone, M., Houser, T., Hsiang, S., Jina, A., Kopp, R.E., Malevich, S.B., McCusker, K.E., Mayer, T., Nath, I., Rising, J., Rode, A., Yuan, J., 2025. Impacts of climate change on global agriculture accounting for adaptation. Nature 642, 644–652. https://doi.org/10.1038/s41586-025-09085-w.

Karger, D.N., Lange, S., Hari, C., Reyer, C.P.O., Conrad, O., Zimmermann, N.E., Frieler, K., 2023. CHELSA-W5E5: daily 1 km meteorological forcing data for climate impact studies. Earth Syst. Sci. Data 15, 2445–2464. https://doi.org/10.5194/essd-15-2445-2023.

Ke, X., Wu, D., Rice, J., Kintner-Meyer, M., Lu, N., 2016. Quantifying impacts of heat waves on power grid operation. Appl. Energ. 183, 504–512. https://doi.org/10.1016/j.apenergy.2016.08.188.

Kendall, M.G., 1975. Rank correlation methods, 4th ed., 2d impression. ed. Griffin, London.

Leahy, P.G., McKeogh, E.J., 2013. Persistence of low wind speed conditions and implications for wind power variability. Wind Energy 16, 575–586. https://doi.org/10.1002/we.1509.

Li, M., Ma, Q., Shan, R., Abdulla, A., Virguez, E., Gao, S., Patiño-Echeverri, D., 2024. Renewable energy quality trilemma and coincident wind and solar droughts. Commun. Earth Environ. 5, 1–14. https://doi.org/10.1038/s43247-024-01850-5.

Liu, F., Sun, F., Liu, W., Wang, T., Wang, H., Wang, X., Lim, W.H., 2019. On wind speed pattern and energy potential in China. Appl. Energy 236, 867–876. https://doi.org/10.1016/j.apenergy.2018.12.056.

Liu, F., Wang, X., Sun, F., Wang, H., 2023a. Wind resource droughts in China. Environ. Res. Lett. 18, 94015. https://doi.org/10.1088/1748-9326/acea35.

Liu, L., He, G., Wu, M., Liu, G., Zhang, H., Chen, Y., Shen, J., Li, S., 2023b. Climate change impacts on planned supply–demand match in global wind and solar energy systems. Nat. Energy 8, 870–880. https://doi.org/10.1038/s41560-023-01304-w.

Lledó, L., Bellprat, O., Doblas-Reyes, F.J., Soret, A., 2018. Investigating the Effects of Pacific Sea Surface Temperatures on the Wind Drought of 2015 over the United States. J. Geophys. Res.:atmos. 123, 4837–4849. https://doi.org/10.1029/2017JD028019.

Long, Y., Xu, C., Liu, F., Liu, Y., Yin, G., 2021. Evaluation and projection of wind speed in the arid region of northwest China based on CMIP6. Remote Sens. 13, 4076. https://doi.org/10.3390/rs13204076.

Lu, X., McElroy, M.B., Kiviluoma, J., 2009. Global potential for wind-generated electricity. Proc. Natl. Acad. Sci. 106, 10933–10938. https://doi.org/10.1073/pnas.0904101106.

Lubega, W.N., Stillwell, A.S., 2018. Maintaining electric grid reliability under hydrologic drought and heat wave conditions. Appl. Energ. 210, 538–549. https://doi.org/10.1016/j.apenergy.2017.06.091.

Lundberg, S., Lee, S.-I., 2017. A Unified Approach to Interpreting Model Predictions. https://doi.org/10.48550/arXiv.1705.07874.

Lundberg, S.M., Erion, G.G., Lee, S.-I., 2019. Consistent Individualized Feature Attribution for Tree Ensembles. https://doi.org/10.48550/arXiv.1802.03888.

Mann, H.B., 1945. Nonparametric tests against trend. Econometrica 13, 245–259.

McElroy, M.B., Lu, X., Nielsen, C.P., Wang, Y., 2009. Potential for wind-generated electricity in China. Science 325, 1378–1380. https://doi.org/10.1126/science.1175706.

Minola, L., Zhang, G., Ou, T., Kukulies, J., Curio, J., Guijarro, J.A., Deng, K., Azorin-Molina, C., Shen, C., Pezzoli, A., Chen, D., 2024. Climatology of near-surface wind speed from observational, reanalysis and high-resolution regional climate model data over the Tibetan Plateau. Clim. Dyn. 62, 933–953. https://doi.org/10.1007/s00382-023-06931-3.

Miralles, D.G., Gentine, P., Seneviratne, S.I., Teuling, A.J., 2019. Land–atmospheric feedbacks during droughts and heatwaves: state of the science and current challenges. Ann. N. Y. Acad. Sci. 1436, 19–35. https://doi.org/10.1111/nyas.13912.

Mitchell, R., Adinets, A., Rao, T., Frank, E., 2018. XGBoost: scalable GPU accelerated learning. doi:10.48550/arXiv.1806.11248.

Molina, M.O., Gutiérrez, C., Ortega, M., Sánchez, E., 2023. Summer heatwaves, wind production and electricity demand in Southern Europe: climatic conditions and impacts. Environ. Res. Commun. 5, 085005. https://doi.org/10.1088/2515-7620/acec37.

Molnar, C., 2022. Interpretable machine learning: a guide for making black box models explainable. Independently published, Munich, Germany.

Nabizadeh, E., Hassanzadeh, P., Yang, D., Barnes, E.A., 2019. Size of the atmospheric blocking events: scaling law and response to climate change. Geophys. Res. Lett. 46, 13488–13499. https://doi.org/10.1029/2019GL084863.

Novick, K.A., Ficklin, D.L., Stoy, P.C., Williams, C.A., Bohrer, G., Oishi, A.C., Papuga, S. A., Blanken, P.D., Noormets, A., Sulman, B.N., Scott, R.L., Wang, L., Phillips, R.P., 2016. The increasing importance of atmospheric demand for ecosystem water and carbon fluxes. Nat. Clim. Chang. 6, 1023–1027. https://doi.org/10.1038/nclimate3114.

Perera, A.T.D., Nik, V.M., Chen, D., Scartezzini, J.-L., Hong, T., 2020. Quantifying the impacts of climate change and extreme climate events on energy systems. Nat. Energy 5, 150–159. https://doi.org/10.1038/s41560-020-0558-0.

Perkins-Kirkpatrick, S.E., Lewis, S.C., 2020. Increasing trends in regional heatwaves. Nat. Commun. 11, 3357. https://doi.org/10.1038/s41467-020-16970-7.

Power Sector Roundtable, 2023. Enhancing Power System Adequacy considering climate risk: Pathways and Mechanisms [WWW Document]. accessed 3.23.25. http://www.nrdc.cn/Public/uploads/2023-07-26/64c0be50d6865.pdf.

Pryor, S.C., Barthelmie, R.J., Bukovsky, M.S., Leung, L.R., Sakaguchi, K., 2020. Climate change impacts on wind power generation. Nat. Rev. Earth. Environ. 1, 627–643. https://doi.org/10.1038/s43017-020-0101-7.

Shmelev, S.E., Salnikov, V., Turulina, G., Polyakova, S., Tazhibayeva, T., Schnitzler, T., Shmeleva, I.A., 2021. Climate change and food security: the impact of some key variables on wheat yield in Kazakhstan. Sustainability 13, 8583. https://doi.org/10.3390/su13158583.

Speizer, S., Raymond, C., Ivanovich, C., Horton, R.M., 2022. Concentrated and intensifying humid heat extremes in the IPCC AR6 Regions. Geophysical Research Letters 49, e2021GL097261. https://doi.org/10.1029/2021GL097261.

Still, C.J., Sibley, A., DePinte, D., Busby, P.E., Harrington, C.A., Schulze, M., Shaw, D.R., Woodruff, D., Rupp, D.E., Daly, C., Hammond, W.M., Page, G.F.M., 2023. Causes of widespread foliar damage from the June 2021 pacific northwest heat dome: more heat than drought. Tree Physiol. 43, 203–209. https://doi.org/10.1093/treephys/tpac143.

Su, B., Huang, J., Fischer, T., Wang, Y., Kundzewicz, Z.W., Zhai, J., Sun, H., Wang, A., Zeng, X., Wang, G., Tao, H., Gemmer, M., Li, X., Jiang, T., 2018. Drought losses in China might double between the 1.5 °C and 2.0 °C warming. Proc. Natl. Acad. Sci. 115, 10600–10605. https://doi.org/10.1073/pnas.1802129115.

Sun, J., Wang, Y., He, Y., Cui, W., Chao, Q., Shan, B., Wang, Z., Yang, X., 2024. The energy security risk assessment of inefficient wind and solar resources under carbon neutrality in China. Appl. Energy 360, 122889. https://doi.org/10.1016/j.apenergy.2024.122889.

Tobin, I., Greuell, W., Jerez, S., Ludwig, F., Vautard, R., van Vliet, M.T.H., Bréon, F.-M., 2018. Vulnerabilities and resilience of European power generation to 1.5 °C, 2 °C and 3 °C warming. Environ. Res. Lett. 13, 44024. https://doi.org/10.1088/1748-9326/aab211.

Wang, J., Chen, Y., Tett, S.F.B., Stone, D., Nie, J., Feng, J., Yan, Z., Zhai, P., Ge, Q., 2023. Storyline attribution of human influence on a record-breaking spatially compounding flood-heat event. Sci. Adv. doi:10.1126/sciadv.adi2714.

Wang, L., Liu, Y., Zhao, L., Lu, X., Huang, L., Jin, Y., Davis, S.J., Aghakouchak, A., Huang, X., Zhu, T., Qin, Y., 2025. Unraveling climate change-induced compound low-solar-low-wind extremes in China. Natl. Sci. Rev. 12, nwae424. https://doi.org/10.1093/nsr/nwae424.

Wang, Y., Yuan, X., 2023. High temperature accelerates onset speed of the 2022 unprecedented flash drought over the Yangtze River basin. Geophys. Res. Lett. 50, e2023GL105375. https://doi.org/10.1029/2023GL105375.

Wang, Z., Wen, X., Tan, Q., Fang, G., Lei, X., Wang, H., Yan, J., 2021. Potential assessment of large-scale hydro-photovoltaic-wind hybrid systems on a global scale. Renew. Sustain. Energy Rev. 146, 111154. https://doi.org/10.1016/j.rser.2021.111154.

Wu, J., Gao, X., 2013. A gridded daily observation dataset over China region and comparison with the other datasets. Chinese Journal of Geophysics 56, 1102–1111.

Wu, J., Gao, X., Giorgi, F., Chen, D., 2017. Changes of effective temperature and cold/hot days in late decades over China based on a high resolution gridded observation dataset. Int. J. Climatol. 37, 788–800. https://doi.org/10.1002/joc.5038.

Wu, J., Zha, J., Zhao, D., Yang, Q., 2018. Changes in terrestrial near-surface wind speed and their possible causes: an overview. Clim. Dyn. 51, 2039–2078. https://doi.org/10.1007/s00382-017-3997-y.

Xu, L., Feng, K., Lin, N., Perera, A.T.D., Poor, H.V., Xie, L., Ji, C., Sun, X.A., Guo, Q., O'Malley, M., 2024. Resilience of renewable power systems under climate risks. Nat. Rev. Electr. Eng. 1, 53–66. https://doi.org/10.1038/s44287-023-00003-8.

Xu, Y., Gao, X., Shen, Y., Xu, C., Shi, Y., Giorgi, F., 2009. A daily temperature dataset over China and its application in validating a RCM simulation. Adv. Atmos. Sci. 26, 763–772. https://doi.org/10.1007/s00376-009-9029-z.

Yan, Y., Li, B., Dechant, B., Xu, M., Luo, X., Qu, S., Miao, G., Leng, J., Shang, R., Shu, L., Jiang, C., Wang, H., Jeong, S., Ryu, Y., Chen, J.M., 2025. Plant traits shape global spatiotemporal variations in photosynthetic efficiency. Nat. Plants 1–11. https://doi.org/10.1038/s41477-025-01958-2.

You, J., Wang, S., 2021. Higher probability of occurrence of hotter and shorter heat waves followed by heavy rainfall. Geophys. Res. Lett. 48, e2021GL094831. https://doi.org/10.1029/2021GL094831.

You, J., Wang, S., Zhang, B., 2024. Spatially seamless and temporally continuous assessment on compound flood risk in Hong Kong. Journal of Hydrology 645, 132217. https://doi.org/10.1016/j.jhydrol.2024.132217.

You, J., Yin, F., Gao, L., 2025. Escalating wind power shortages during heatwaves. Commun. Earth Environ. 6, 245. https://doi.org/10.1038/s43247-025-02239-8.

Zhao, J., Li, F., Zhang, Q., 2024. Impacts of renewable energy resources on the weather vulnerability of power systems. Nat. Energy 1–8.

Zhou, B., Hu, S., Peng, J., Li, D., Ma, L., Zheng, Z., Feng, G., 2023. The extreme heat wave in China in August 2022 related to extreme northward movement of the eastern center of SAH. Atmos. Res. 293, 106918. https://doi.org/10.1016/j.atmosres.2023.106918.

Zhu, L., Wang, Y., Chavas, D., Johncox, M., Yung, Y.L., 2024. Leading role of Saharan dust on tropical cyclone rainfall in the Atlantic basin. Sci. Adv. 10. https://doi.org/10.1126/sciadv.adn6106.

Zhuo, C., Junhong, G., Wei, L., Fei, Z., Chan, X., Zhangrong, P., 2022. Changes in wind energy potential over china using a regional climate model ensemble. Renew. Sustain. Energy Rev. 159, 112219. https://doi.org/10.1016/j.rser.2022.112219.